Modeling and High-Definition Control of a Smart Electroadhesive Actuator: Toward Application in Rehabilitation

Navid Feizi, *Graduate Student Member, IEEE*, S. Farokh Atashzar, *Senior Member, IEEE*, Mehrdad R. Kermani, *Member, IEEE*, and Rajni V. Patel, *Life Fellow, IEEE*

***Abstract*—Smart actuators with tunable dynamical characteristics have shown significant potential to improve the performance of physical human-robot interaction systems, such as exoskeletons. In this regard, electroadhesive clutches, which function based on a controllable dry kinetic friction between the discs, have attracted a great deal of interest for semi-passive actuation that has a high force-to-weight ratio and low power consumption. However, the complex dynamical behavior of such an actuator has limited the potential application in dynamic tasks. This paper, for the first time, presents a robust nonlinear control law for torque-adjustable rotary electroadhesive clutches in order to guarantee smooth, agile, and stable behavior in the presence of significant unmodeled dynamics. For this, a nonlinear Lyapunov-redesign approach is proposed based on a partially-identified model, which can guarantee convergence and robustness to unmodeled dynamics. The performance of the proposed algorithm is validated through a comprehensive set of experiments, including active-resistive and coordination-assisted rehabilitation using an elbow exoskeleton designed based on the rotary electroadhesive clutch. The proposed approach shows potential for application in dynamic scenarios such as those involving assistive and wearable robots.**

Manuscript received 8 June 2022; revised 13 August 2022 and 11 October 2022; accepted 13 October 2022. Date of publication 25 October 2022; date of current version 21 November 2022. This article was recommended for publication by Associate Editor L. Ricotti and Editor P. Dario upon evaluation of the reviewers' comments. The work of S. Farokh Atashzar was supported by the U.S. National Science Foundation under Grant 2121391. The work of Mehrdad R. Kermani was supported in part by the Natural Sciences and Engineering Research Council (NSERC) of Canada under Grant RGPIN-06253, and in part by the Western Strategic Support for NSERC through the Seed and Accelerator Program. The work of Rajni V. Patel was supported in part by the Natural Sciences and Engineering Research Council (NSERC) of Canada under Grant RGPIN-1345, and in part by the Canada Research Chairs Program. *(Corresponding author: Navid Feizi.)*

Navid Feizi is with the Canadian Surgical Technologies and Advanced Robotics, Lawson Health Research Institute, London, ON N6A 5A5, Canada, and also with the School of Biomedical Engineering, Western University, London, ON N6A 3K7, Canada (e-mail: feizi@uwo.ca).

S. Farokh Atashzar is with the Department of Electrical and Computer Engineering, Mechanical and Aerospace Engineering, Biomedical Engineering, New York University, New York, NY 11201 USA, also with NYU WIRELESS Center, Brooklyn, NY 11201 USA, and also with NYU CUSP, Brooklyn, NY 11201 USA (e-mail: sfa7@nyu.edu).

Mehrdad R. Kermani is with the Department of Electrical and Computer Engineering, Western University, London, ON N6A 5B9, Canada (e-mail: mkermani@eng.uwo.ca).

Rajni V. Patel is with the Canadian Surgical Technologies and Advanced Robotics, London Health Sciences Centre, London, ON N6A 5A5, Canada, and also with the Department of Electrical and Computer Engineering, the Department of Surgery, the Department of Clinical Neurological Sciences, and the School of Biomedical Engineering, Western University, London, ON N6A 5B9, Canada (e-mail: rvpatel@uwo.ca).

Digital Object Identifier 10.1109/TMRB.2022.3216906

***Index Terms*—Electroadhesion, smart actuators, adjustable clutch, robust control.**

I. Introduction

With the development of collaborative robotics, rehabilitation robots, exoskeletons, and in general, robots that share physical workspace with humans, safety has become critically important in order to ensure safe physical human-robot interaction (pHRI) [1]. At present, there are several applications where robots work alongside humans, such as monitoring and assistance, rehabilitation, and surgery [2], [3], [4], [5], [6], [7]. A key requirement in such applications is that the safety of the humans involved in the interaction should not be compromised [8], [9]. The need for high speed and high force actuation, which is frequently required for effective performance of the robot, has been fulfilled in the literature by designing high impedance actuators. However, the use of an actuator with high impedance in pHRI can give rise to major safety concerns. Thus, future generations of human-safe robots will depend on developing new actuation technologies that can offer inherent safety [10].

The Series Elastic Actuator (SEA) is considered a reliable actuator designed for applications that involve interaction with unknown dynamics, such as those in pHRI, e.g., an SEA has been used for actuation of a knee exoskeleton [11]. Although SEA provides intrinsic passive compliance due to its elasticity, it is not adjustable, thus limiting its range of applications. Variable Impedance Actuators (VIA) enable adjustable compliance through changing stiffness and damping. VIA is used in a broad range of applications, including haptics, assistive devices, rehabilitation, prosthetics, and exoskeletons [12]. These actuators provide higher levels of pHRI safety than conventional actuators since they mechanically decouple the robot's end effector from the high-impedance gear motor.

Semi-passive actuators can guarantee intrinsic safety not only because of the decoupled end effector from the motor but also because of their passive nature. Magneto-rheological (MR) and electro-rheological (ER) clutches are examples of common types of semi-passive actuators. MR clutches provide torque using the viscous friction of the magneto-rheological fluid between the rotor and stator [10], [13], [14]. The amount of viscous friction in these types of clutches is adjusted by manipulating the magnetic field inside

2576-3202 © 2022 IEEE. Personal use is permitted, but republication/redistribution requires IEEE permission.
See https://www.ieee.org/publications/rights/index.html for more information.

Authorized licensed use limited to: New York University. Downloaded on December 23,2022 at 06:14:04 UTC from IEEE Xplore. Restrictions apply.

the clutch. Therefore, a coil is needed inside the clutch to provide the required magnetic field. The need for a coil is the main disadvantage of MR clutches, which makes them heavy and needs high current to generate the required magnetic field. This limits the design parameters and areas of applications, especially in mobile and wearable robotic devices [15], [16]. On the other hand, ER clutches, which are based on the viscous friction of the ER fluid, have been proposed as an alternative approach for the above-mentioned issue in rehabilitation and assistive robotics [17], [18]. This removes the need for a coil since the viscosity of the ER fluid can be tuned using an electric field. ER clutches have been used in multiple assistive and rehabilitation robotics applications. However, the low viscosity of the ER fluid limits the output torque of the clutch. In addition, high voltage (in the range of kV) is required to generate the needed electric field. Another novel approach, but still in its infancy, is the miniaturized MR clutches [19].

The force resulting from electroadhesion (EA) can be generated without the need for heavy parts and high currents. In [20], with a proper selection of a dielectric, a noticeable amount of attraction force was achieved under a relatively low voltage (below 300 volts). This force was harnessed in various applications, mostly to generate friction [21]. The ultra-lightweight and low power consumption of EA have attracted a great deal of interest, mostly in wearable robotics. In [22], miniature EA clutches were employed as a joint locking mechanism in a robotic hand. In [20], [23], a translational lightweight EA clutch was described and used in an ankle exoskeleton. EA was used as a braking mechanism for a 2.5D haptics display [24]. A high force density wearable EA clutch was utilized in [25] for haptic gloves. A wearable linear EA clutch was developed and implemented in an elbow haptic device [26], [27]. A feasibility analysis of a rotational EA clutch was presented in [28]. An adaptive damper using EA was developed in [29]. Except in [29], the above-mentioned EA actuators were implemented in on/off mode in the form of a locking mechanism by utilizing static friction without the ability to tune the actuation force/torque.

The lack of research on adjustable EA clutches may be due to the issue of the space charge build-up in the friction interface, as reported in [22], [24], [25], [30], [31], [32] and our previous work [33]. The space charge build-up in the dielectric causes the degradation of the attraction force when the clutch is activated. In addition, it creates a residual force when the clutch is disengaged after an active period. These issues complicate the modeling of EA clutches, especially when the underlying force generation mechanism of the clutch is through sliding friction [30]. In this paper, a novel approach is proposed for electroadhesion regulation of an EA clutch using pulse-width modulation (PWM) with positive and negative magnitudes. This eliminates not only residual electroadhesion [24], [30] but also maintains steady force. In this paper, we implemented this method on a rotary electroadhesive clutch as an example. The proposed electroadhesion modulation enables easy adjustment of the clutch torque by tuning the activation signal duty cycle. Additionally, we propose a robust control (RC) method for controlling the clutch torque and increasing the actuation bandwidth. We validate the performance of the EA clutch, including the proposed RC in active-resistive and coordination-assisted [34], [35] robotic rehabilitation scenarios using an elbow exoskeleton designed based on the EA clutch. The main contributions of the paper are:

- Modeling of the friction characteristics of the dielectric.
- Proposing a positive and negative magnitude PWM signal to adjust the electroadhesion, and mitigating the electroadhesion degradation due to charge accumulation on the dielectric surface.
- Developing novel nonlinear as well as linear output torque models.
- Validating high-fidelity torque control using RC in active-resistive and coordination-assisted rehabilitation scenarios.

The proposed clutch is applicable for high force-to-weight and low-power applications such as mobile assistive and wearable robotics.

The following is an outline of the rest of this document. Section II provides an overview of an EA clutch and the experimental setup. Section III describes the proposed nonlinear pure friction model. Section IV presents the proposed linear and nonlinear models of the clutch. Section V describes the process of RC design and the selection of the appropriate control parameters. Section VI provides experimental results of the RC, as well as comparisons with results achieved through the use of a proportional–integral (PI) controller. Section VII presents two rehabilitation scenarios using the EA clutch including experimental results. Section VIII concludes the paper with final remarks.

II. EA Clutch and the Experimental Setup

The EA clutch transfers force/torque using dry sliding friction between two clutch plates. When high voltage is applied across the clutch plates, the electroadhesion due to the static charges on the clutch plates creates a strong attraction force. A dielectric is used between the plates to provide electric isolation and prevent electric discharge. Therefore, an attraction force can be maintained when a high voltage is applied across the plates. This normal force due to electroadhesion leads to friction that couples the motion of the input and output clutch plates (see [23] for detail).

In this paper, we used a rotary EA clutch to verify the performance of the proposed method. The core of the rotary EA clutch is comprised of: (1) two rotor discs; (2) a stator disc (rotor and stator discs are made of 0.1 mm thick 1095 Spring steel (McMaster-Carr, ON, Canada)); and (3) a machined splined rotary shaft (see Fig. 1). The thickness of the discs and their material are selected such that they provide enough flexibility for the disc in the axial direction to fill the air gap between the rotor and the stator under electroadhesion while providing enough stiffness in the tangential direction to transfer torque. The rotor discs are mounted on the clutch housing and the output of the drive motor of the test-setup. Rotors are mounted such that they rotate with the housing, but they can slide axially to fill the air gap between discs, as shown in Fig. 1. The stator disc, which is sandwiched between two rotor discs, is mounted on the output shaft using

Authorized licensed use limited to: New York University. Downloaded on December 23,2022 at 06:14:04 UTC from IEEE Xplore. Restrictions apply.

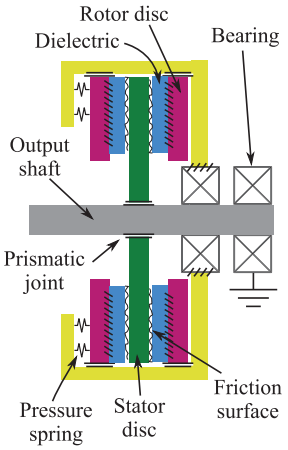

Fig. 1. Schematic of the rotary electroadhesive clutch.

a 3D printed connecting part, which transfers the torque from the disc to the shaft while enabling it to slide axially on the shaft. The rotor discs were coated with 95 μm DuPont 8153 dielectric before being cut to shape using electric discharge machining. The coating procedure was done through application of five layers of the dielectric film to reach the expected thickness [23].

An ideal separation between the stator and the rotor discs is to be maintained so that friction and wear of the discs can be avoided when the clutch is disengaged. However, keeping a zero gap between the discs will maximize the EA forces and the clutch response time. In order to address these two competing design requirements, pressure springs were utilized to apply enough pressure to minimize the air gap while avoiding significant friction when the clutch is in free motion.

The rotor discs have an inner radius of 4 cm and the stator disc has an outer radius of 6 cm, creating a ring-shaped friction area of the same inner and outer radii. Details of the design of the rotary clutch with one friction surface are given in [33]. However, in this research, two rotor discs and both sides of the stator disc were used to double the friction area and maximize torque. The formulation of the maximum torque is as follows:

$$T = \frac{2\pi\left(r_2^3 - r_1^3\right)\sigma_{sh} n}{3} \tag{1}$$

where r_1 and r_2 are the inner and outer radii of the friction ring, σ_{sh} is the shear stress, and n is the number of friction surfaces, which is equal to 2 in this design.

A custom high-voltage driver circuit was used to activate the EA clutch. The main components of the driver circuit are: (1) a PHV 12 DC-DC high voltage transformer (Bellnix Co., Saitama, Japan); (2) a high-voltage H-Bridge made of IKW50N65 IGBTs (Infineon Technologies, Neubiberg, Germany), to enable activation of the clutch under PWM signal; and (3) an Arduino to interface the driver to the computer. Data acquisition and control were done in real-time with the loop frequency of 1 kHz using QuaRC real-time control software (Quanser, ON, Canada) in the MATLAB Simulink environment. The driver circuit gets the amplitude, frequency, and duty cycle of the target PWM signal from the computer through the serial bus. Fig. 2 shows one period of the generated signal along with the expected ideal torque. The duty

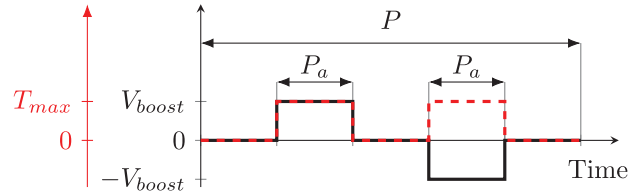

Fig. 2. A sample of a period of the positive and negative magnitudes PWM signal and expected clutch torque. The black graph shows the control signal. The dashed red graph shows the instantaneous expected torque.

cycle of the PWM signal calculates as follows:

$$Duty\ cycle = \frac{2P_a}{P} \tag{2}$$

where P_a is the duration of the positive value of the PWM signal in a period, which is equal to the duration of the negative value of the signal in the same period and P is the period of the PWM signal.

The frequency of the PWM signal is selected as 300 Hz in all experiments. An ATI Gamma sensor is connected to the output shaft of the clutch to measure the feedback torque.

III. Friction Modeling

In this section, the characteristics of the friction between the clutch discs (which is the dielectric against steel) for one friction interface are investigated. This has been done by analyzing the effect of the normal force and the rotation velocity on the torque. A kinetic friction model mapping the normal force to the output torque of the clutch is proposed.

In order to measure the friction, the electroadhesion part of the clutch is bypassed and a constant normal force is applied to push the discs together using weights. This was done utilizing a lever mechanism with an advantage ratio of 4.33 to amplify the force due to weights.

A. Normal Force Effect

In order to evaluate the effect of the normal force, each experiment was carried out under a constant rotation velocity of 15 RPM. Different normal forces ranging from 17 to 170 N (equivalent to stress ranging from 2.7 to 27 kPa) were applied on the discs. For the sake of brevity, only some of the recorded data are shown in Fig. 3. As can be seen, the torque demonstrates a dynamic behavior which can be partially due to the stiffness of the system components, including rotating parts and the lever mechanism. However, most of the dynamic behavior of the torque is due to the friction interface.

A function comprised of two exponentials, as below, is proposed to model the torque due to friction shown in Fig. 3.

$$T(t,f) = \left(C\left(1 - e^{\frac{-t}{\tau_1(f)}}\right) + (1-C)\left(1 - e^{\frac{-t}{\tau_2(f)}}\right)\right) T_s(f) \tag{3}$$

In (3), the first term in the parentheses is related to the fast dynamics of friction and the second term is associated with the slow dynamics, t denotes time, f is the normal force, T_s is the torque achieved at the end of each experiment, τ_1 and τ_2 are time constants, and C is the factor that adjusts the portion of the fast dynamics. To identify the model parameters, (3) is fitted to the recorded data for each experiment using sequential

Authorized licensed use limited to: New York University. Downloaded on December 23,2022 at 06:14:04 UTC from IEEE Xplore. Restrictions apply.

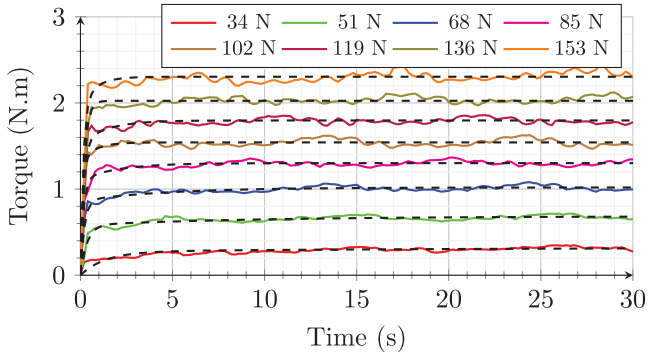

Fig. 3. The solid lines illustrate the experimental torque vs. time for different normal forces. The normal force is applied at t = 0. The dashed lines show the estimated torque associated with each normal force using the proposed friction model.

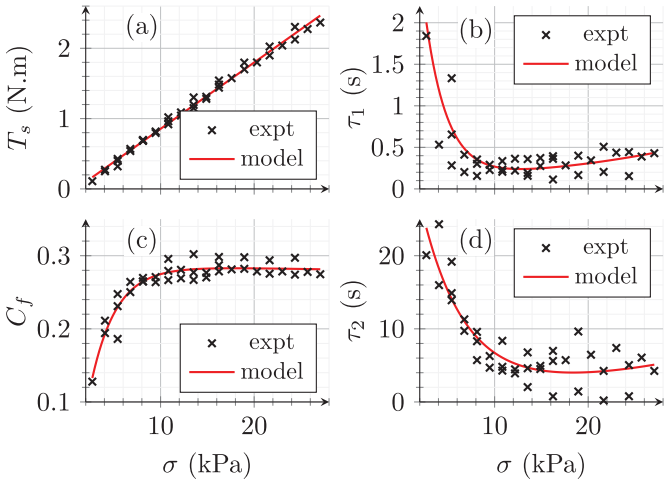

Fig. 4. Identified parameters of the friction model. The graphs show the variation of (a) Stable torque. (b) τ_1. (c) Friction coefficient. (d) τ_2.

TABLE I
IDENTIFIED PARMETERS OF THE STRESS-BASED FRICTION MODEL

parameter	model	fit rmse
T_s	$0.0944\Omega - 0.0896$	0.323
C_f	$0.29e^{-0.000725\Omega} - 0.42e^{-0.337\Omega}$	0.0127
τ_1	$6.01e^{-0.431\Omega} + 0.11e^{0.0492\Omega}$	0.277
τ_2	$40.25e^{-0.219\Omega} + 1.37e^{0.0476\Omega}$	2.67

quadratic programming (SQP). In order to reduce the degree of freedom of the problem and avoid overfitting, a constant value 0.85 is selected for C through observations. T_s, τ_1, and τ_2 are determined as shown in Fig. 4 for each experiment. The model parameters are show in Table I. From Fig. 4(b) and Fig. 4(d) it can be seen that the torque dynamics are sluggish under smaller normal stresses. However, when the stress increases, τ_1 and τ_2 reduce to around 0.3 and 4 seconds, respectively. This means that friction increases up to 85% with a time constant of 0.3 s, and the rest of the torque will be achieved with slower dynamics with a time constant of 4 s.

Fig. 4(c) shows the coefficient of friction. As can be seen in the figure, within the observed range, the coefficient of friction C_f increases with the increase of the normal stress and reaches

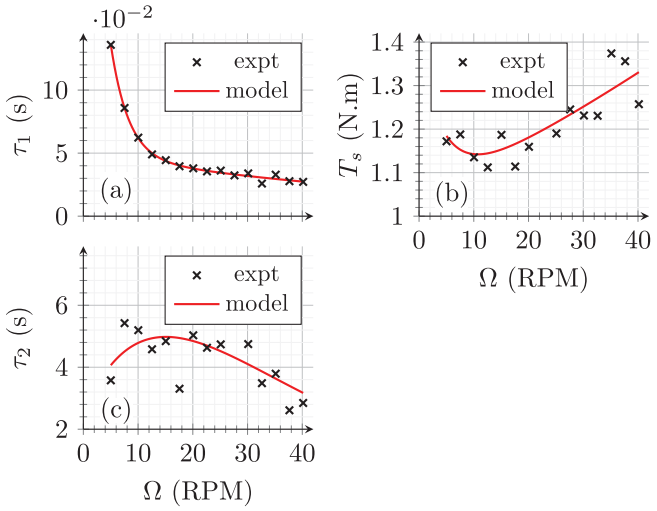

Fig. 5. Identified parameters of friction model. The graphs show the variation of (a) τ_1. (b) Stable torque. (c) τ_2.

a saturated value. This effect might be due to the imperfect friction surface, which prevents engagement of the full area of the discs, leading to a smaller effective friction area. However, as the rotor disc is designed to be flexible, it deflects and fills the gaps when normal stress increases resulting in a more effective friction surface and, thus a higher friction coefficient.

B. Velocity Effect

One of the factors affecting friction is sliding velocity. In order to investigate this effect, a series of experiments were conducted in which the clutch was rotated with a constant velocity for 60 s and a constant normal force of 86 N was applied on the discs. This experiment was repeated for velocities ranging from 5 to 40 RPM.

Fig. 5(b) shows the achieved maximum torque for different rotation velocities. The red line shows the second-order exponential model fitted to the experimental data using SQP algorithm. Parameters of the fitted model are shown in Table II. As can be seen in the figure, when the velocity is below 12 RPM, the torque reduces with the increase of the velocity; however, the torque increases almost linearly with the increase of the velocity when the velocity is above 12 RPM. This is mainly because of the viscous component of friction [36]. Fig. 5(a) and Fig. 5(c) show the identified time constants for different velocities. Comparing the order of variations of τ_1 and τ_2 in Fig. 5 with the same in Fig. 4, it can be seen that the effect of the rotation velocity on the dynamics of the torque is noticeably less than the effect of the normal force. From the small variation of the time constant with change in velocity, it can be inferred that the stiffness of the rotating components is not a major contributor to the whole dynamics of the system.

IV. CLUTCH MODEL IDENTIFICATION

The EA clutch can be activated under direct current (DC) or alternating current (AC), each of which exhibits a unique behavior. Utilizing DC activation signal leads to space charge

Authorized licensed use limited to: New York University. Downloaded on December 23,2022 at 06:14:04 UTC from IEEE Xplore. Restrictions apply.

TABLE II
IDENTIFIED PARMETERS OF THE VELOCITY-BASED FRICTION MODEL

parameter	model	fit rmse
T_s	$0.349e^{-0.230\Omega} + 1.042e^{0.00608\Omega}$	0.0523
τ_1	$0.425e^{-0.310\Omega} + 0.0498e^{-0.0150\Omega}$	0.0020
τ_2	$5.375 \times 10^5 e^{-0.0507\Omega} - 5.374 \times 10^5 e^{-0.0507\Omega}$	0.850

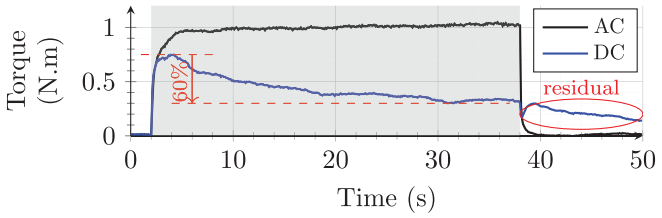

Fig. 6. Output torque under DC and AC activations. The active region is shaded in gray [33].

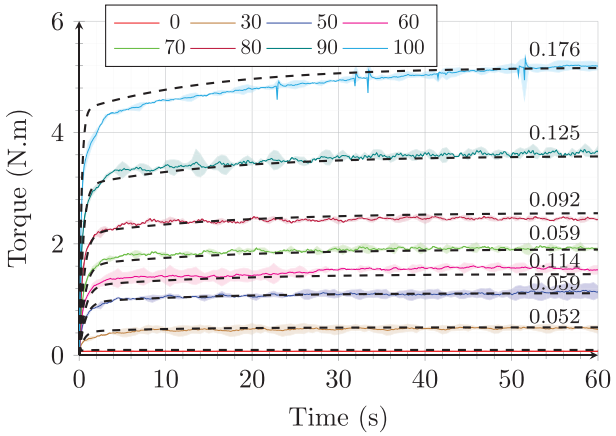

Fig. 7. Averaged experimental values (solid lines), standard deviation (highlighted areas), and the predicted torques using the proposed nonlinear model (dashed lines) for different input signals vs. time. The legend shows the PWM duty cycle value. The written value close to each graph shows the RMSE of model estimation for each input signal. The amplitude of the input PWM signal was 300 V.

build-up in the dielectric [31], [33]. The accumulated charges create an electric field counteracting the electric field generated by the charges on the disc. The dynamics of formation and degradation of the space charges in the dielectric are much slower than those of the electric charges on the conductive part of the discs. Thus, it causes torque degradation with the passage of time when the clutch is engaged. It also causes undesirable residual torque after the onset of deactivation of the clutch (see Fig. 6). Both of the above-mentioned issues were addressed by using AC activation signals [33]. Thus, in this paper, only AC activation is considered for modeling and control. In this section, a nonlinear and a linear model are proposed to map the control signal to torque.

A. Nonlinear Model

Prior to model identification, an experiment was carried out to measure the torque variation with time as a function of the control signal (PWM duty cycle). In the experiment, the clutch was rotated with a constant velocity of 10 RPM for 10 seconds while being idle (i.e., no activation). Then it was activated with 600 V peak-to-peak bipolar PWM signal (see Fig. 2). To achieve the desired voltage, the duty cycle was increased to the target value with a step function. This procedure was repeated for duty cycles ranging from 10 to 100 (condescending to the activation voltage of 60 V to 600 V). Each experiment was repeated three times, and the average values were used for model identification. Fig. 7 shows the average of the measured values along with their standard deviation. Since the output torque did not vary significantly in smaller duty cycles, the results for the lower duty cycles are eliminated for the sake of brevity. A nonlinear model, given in (4), was fitted to the recorded values using the SQP algorithm.

$$T(t,u) = \left(C\left(1 - e^{\frac{-t}{\tau_1(u)}}\right) + (1-C)\left(1 - e^{\frac{-t}{\tau_2(u)}}\right)\right) T_s(u) \quad (4)$$

The model given in (4) and its parameters are the same as those in (3). The only difference is the input u, which represents the control signal instead of the normal force. The variations of τ_1, τ_2, and T_s with respect to the control signal are modeled using polynomials of orders 2, 2, and 3, respectively, as given below:

$$\tau_1(u) = a_2u^2 + a_1u + a_0 \quad (5)$$
$$\tau_2(u) = b_2u^2 + b_1u + b_0 \quad (6)$$
$$T_s(u) = c_3u^3 + c_2u^2 + c_1u + c_0 \quad (7)$$

TABLE III
IDENTIFIED PARAMETERS OF THE NONLINEAR CLUTCH MODEL

symbol	value	symbol	value
a0	6.74×10^{-3}	c0	-1.19×10^{-2}
a1	2.39×10^{-2}	c1	1.81×10^{-3}
a2	-2.13×10^{-4}	c2	-2.97×10^{-5}
b0	0.93	c3	1.85×10^{-7}
b1	0.41	C	0.85
b2	-2.64×10^{-3}		

The identified parameters of the proposed nonlinear model in (4) are shown in Table III. The overall absolute estimation error of the proposed nonlinear model is 0.065 ± 0.059 N.m. The estimated torque with respect to time using the nonlinear model and the estimation error of the model for each input signal are shown in Fig. 7. It can be seen that the nonlinear model follows the experimental results accurately.

B. Linear Model Estimation

The model in (4) describes the torque variation with time and control signal. However, the complexity of the model increases the computational cost of the controller. Thus, a simplified first-order linear model is proposed as shown below:

$$\dot{T} = -a_0T + b_0u + c_0 \quad (8)$$

where T is the torque, u is the control signal, a_0, b_0, and c_0 are the model parameters that are identified using the SQP algorithm, which are equal to 1.36, 0.08, and -2.42, respectively. The estimated torque and associated experimental values are shown in Fig. 8. As can be seen, the linear model can only estimate the output torque accurately when the control signal

Authorized licensed use limited to: New York University. Downloaded on December 23,2022 at 06:14:04 UTC from IEEE Xplore. Restrictions apply.

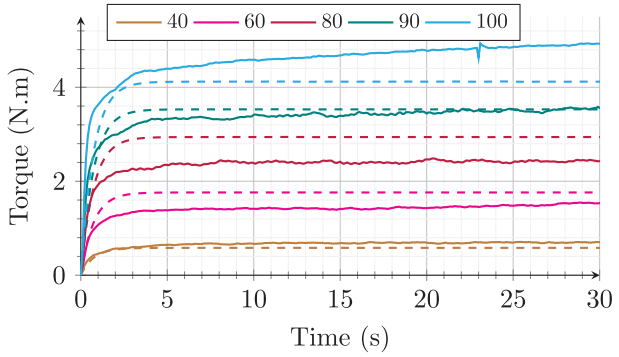

Fig. 8. Clutch torque for different control signals. The legend shows the PWM duty cycle value. The clutch was activated at t = 0 s. Solid lines illustrate the experimental torque. Dashed lines show the estimated torque calculated using the linear model.

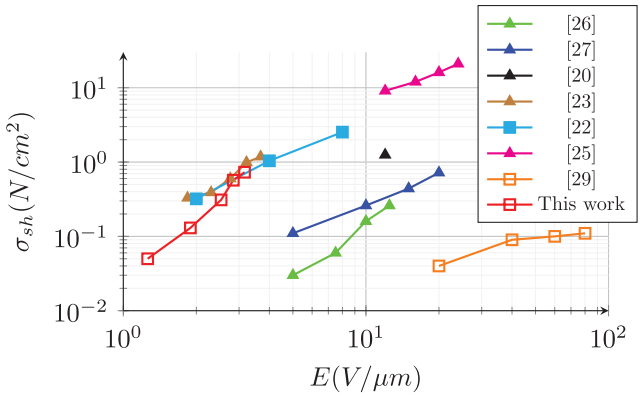

Fig. 9. Friction shear stress vs. applied electric field for the EA actuators in the literature and our EA clutch. The triangle markers show linear actuators, and the square markers show rotational actuators. The hollow markers demonstrate adjustable actuators.

is close to 40 or 90. This straightforward model is used for the implementation of an RC in the rest of the paper.

Fig. 9 shows the friction shear stress vs. electric field for the prominent EA actuator presented in the literature along with our clutch. As can be seen, the shear stress per electric field achieved in our design is close to the maximum value reported in [22], [23], which is remarkably higher than the shear stress reported in [20], [26], [27], [29]. It should be noted that, in contrast with the locking actuators presented in the literature, which work based on static friction, our clutch is adjustable and works based on sliding friction, which is naturally lower than static friction [36].

V. Robust Controller Design

In this section, an RC based on the linear model identified in (8) is implemented to control the output torque of the clutch. Although the nonlinear model in (4) better addresses the variations in the torque in comparison to the linear model, the implementation of a controller based on the nonlinear model is computationally intensive and increases the complexity of the control system. Thus, the linear model is used in the controller design procedure. However, the linear model contains uncertainties due to the linearization, unmodeled dynamics, and intrinsic uncertainties resulting from friction. In order to compensate for the uncertainties of the system and guarantee performance, the Lyapunov function redesign approach [37], [38] was used in this paper. The performance of the proposed controller is compared with that of a PI controller.

A. Robust Controller

In order to make the model compatible with the controller design procedure [38], we consider our torque control problem similar to a joint velocity control problem. By substituting the torque variable T with its counterpart, the joint velocity variable $\dot{q}$, (8) can be written as,

$$B(q)\ddot{q} + \eta(q, \dot{q}) = u \tag{9}$$

where $B = \frac{1}{b_0}$ and $\eta = \frac{1}{b_0}(a_0\dot{q} - c_0)$. Since, there are uncertainties in the model parameters B and, we rewrite (9) as,

$$\hat{B}(q)\ddot{q} + \hat{\eta}(q, \dot{q}) = u \tag{10}$$

where $\hat{B}$ ans $\hat{\eta}$ are the estimated values for B and η. Following the standard inverse dynamics control approach, one can obtain the non-linear control law using (10) as follows:

$$u = \hat{B}y + \hat{\eta}(q, \dot{q}) \tag{11}$$

where

$$y = \ddot{q}_d + K_D\dot{\tilde{q}} + K_P\tilde{q} + \omega \tag{12}$$

in that $\ddot{q}_d$ is the feedforward desired signal, $\tilde{q} = q_d - q$ is the error, and K_P and K_D are the proportional-derivative (PD) controller design parameters. It should be noted that according to the $\dot{q} = T$ analogy, the PD controller implemented on the variable q is equivalent to a PI controller on the actual clutch output T. In (12), the PD term $K_D\dot{\tilde{q}}+K_P\tilde{q}$ ensures stabilization of the error dynamics and the term ω provides the robustness of the controller against a predefined range of uncertainties in model estimation (see [38] for detail).

In an ideal scenario, the control law $\omega = \frac{\rho}{\|z\|}z$ (where $z = D^TQ\xi$, $D = [0, 1]^T$, Q is a (2n × 2n) positive definite matrix, and $\xi = [\tilde{q}, \dot{\tilde{q}}]^T$) would compensate for the uncertainties. However, in order to avoid the generation of the high-frequency components due to chattering in the control signal, when z converges to zero, and also because of the actuator limitations, the effort of the robust control term is limited to $\frac{\rho}{\epsilon}z$ when z is less than the threshold ϵ. The signal transformation from the above-mentioned control law to its limited value is implemented using a tangent hyperbolic soft switch. Thus, the formulation of the RC law is as follows:

$$\omega = S\frac{\rho}{\|z\|}z + (1 - S)\frac{\rho}{\epsilon}z \tag{13}$$

where

$$S = \frac{tanh\big(\gamma(z - \epsilon)\big) + 1}{2} \tag{14}$$

and γ adjusts the speed of the transition between the fist term and the second term on the right side of (13) - the higher the value of γ the faster the transition.

Using the control law (13), the convergence of the error can be guaranteed through Lyapunov stability theory if the

Authorized licensed use limited to: New York University. Downloaded on December 23,2022 at 06:14:04 UTC from IEEE Xplore. Restrictions apply.

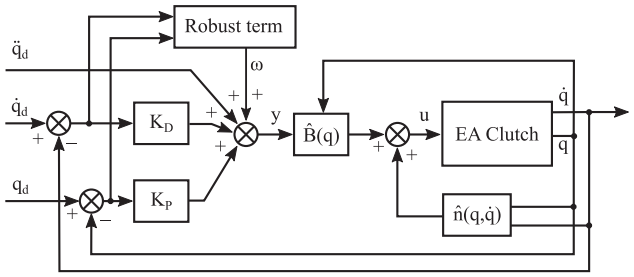

Fig. 10. Block diagram of the robust controller [38].

TABLE IV
IDENTIFIED PARAMETERS OF THE ROBUST CONTROLLER

symbol	value	symbol	value
B_m	12.4	ϵ	0.5
B_M	42.6	γ	50
Q_M	5	K_D	3
ϕ	0.05	K_P	4.5

condition $\rho \geq \|\eta\|$ is satisfied. This can be rewritten as the inequality below [38]:

$$\rho \geq \frac{1}{1-\alpha}\left(\alpha Q_M + \alpha\|K\|\|\xi\| + B_M\phi\right) \tag{15}$$

where

$$\begin{cases} \ddot{q}_d < Q_M & \text{(16a)} \\ \|\eta - \hat{\eta}\| \leq \phi & \text{(16b)} \\ \alpha = \dfrac{B_M - B_m}{B_M + B_m} & \text{(16c)} \end{cases}$$

and B_m and B_M are the lower and upper bounds of the variation of $\hat{B}$, respectively, and $K = [K_P, K_D]$. Fig. 10 shows the block diagram of the control system.

In order to find B_m and B_M, (8) was fitted to the experimental data for each input signal individually; B_m and B_M were estimated to be 12.4 and 42.6, respectively, according to the range of the variations in b_0; Q_M was selected to be 5 based on the range of the accelerations of the expected input trajectory; and ϕ was selected through observation of the performance of the controller. A larger value of ϕ results in a larger control signal [39]. However, due to the limitations of the applicable range of the actuators, increasing ϕ may lead to chattering. Thus, ϕ was selected to be 0.05 to avoid chattering. All controller parameters are shown in Table IV.

B. PI Controller

A PI controller is also implemented to compare with the performance of the RC. Due to the friction-based physics of the EA clutch (a) there is enough damping in the system, (b) there is high-frequency components (due to the sliding of two surfaces of the clutch) which can be amplified by a derivative term. Hence, we use a PI controller to compare it with the robust controller rather than a PID or a PD controller. On the other hand, as mentioned in Section V-A, the integrated PD controller implemented on the variable q in the RC is actually a PI controller on the actual clutch torque T. Therefore, comparing the RC with a PI controller demonstrates the effect of the robust term of the RC. The PI controller parameters are tuned based on the estimated linear model in (8) to reach 1% overshoot and a settling time of to 0.27 s. The calculated control parameters K_P and K_I are determined to be 21 and 360, respectively.

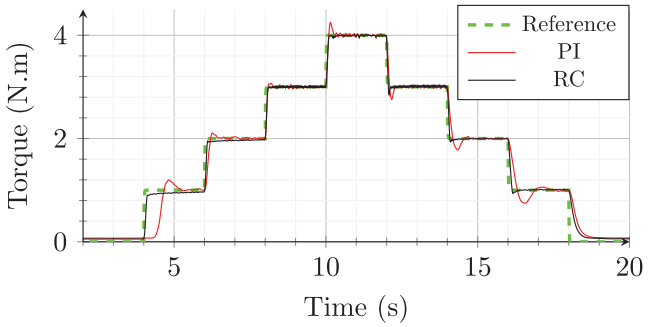

Fig. 11. Step response of the clutch using the RC and PI controller.

VI. CONTROLLER RESULTS AND DISCUSSION

In this section, the performance of the RC is examined and compared with then of the PI controller for different torque trajectories.

In the first experiment, an increasing and decreasing step trajectory ranging from 0 to 4 N.m is used as the reference signal to evaluate the system's performance. Results are shown in Fig. 11. As can be seen in the figure, using the RC resulted in a shorter rise time with negligible overshoot compared to the PI controller. More significantly, the variation in the torque after reaching the reference value in each step, which might be because of the uncertainties due to friction (see torque variation in Fig. 3), is eliminated using the RC. The slow settling time in the last decreasing step is due to the intrinsic sluggish dynamics of the friction under lower normal forces (see Fig. 4(b) and Fig. 4(d)). This cannot be compensated since the actuator is limited to its lower bound.

In order to investigate the controller performance further, a multi-sinusoidal reference trajectory consisting of sinusoidal components with frequencies ranging from 0.2 to 4 Hz is fed to the system. Fig. 12(a) shows the output torques. As can be seen in the figure, the RC tracks the reference signal accurately; however, a phase lag and higher tracking error can be seen for the PI controller. The PI controller phase lag can be because of the relatively larger settling time. However, designing the controller to reach a faster settling time while keeping the control signal within the limited range of the actuator would result in even larger overshoots. The observed overshoot from the experimental data is higher than what the PI is tuned for (1%). This behavior can be explained according to the unmodeled nonlinear dynamics of the clutch. The tracking error is more clearly shown in Fig. 12(b). The amplitude of the tracking error for the RC is limited to 0.2 Nm, which is 83% less than for the PI controller, which is 1.2 Nm. Fig. 12(c) shows the control signal for both controllers.

Sinusoidal reference signals with frequencies ranging from 0.2 to 3 Hz were used to evaluate the frequency response of the clutch with the RC. The same experiment was also repeated

Authorized licensed use limited to: New York University. Downloaded on December 23,2022 at 06:14:04 UTC from IEEE Xplore. Restrictions apply.

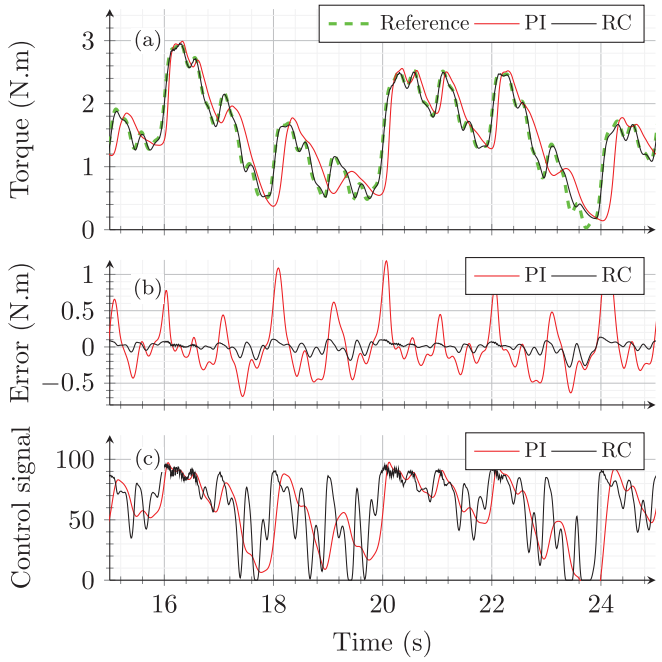

Fig. 12. Demonstration of the performance of the RC and PI controller for a multi-sinusoidal trajectory comprised of harmonics ranging from 0.2 to 4 Hz. (a) Torque. (b) Torque tracking error. (c) Control signal.

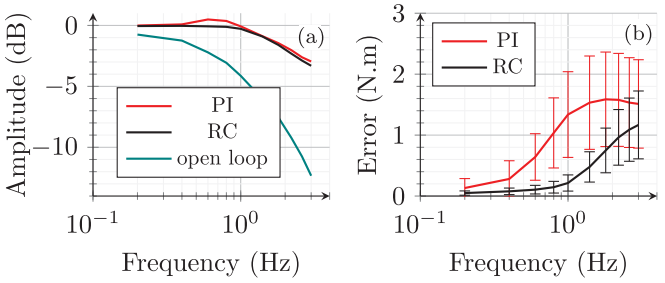

Fig. 13. Results of the frequency response. (a) Amplitude of the response (dB). (b) Absolute tracking error (N.m).

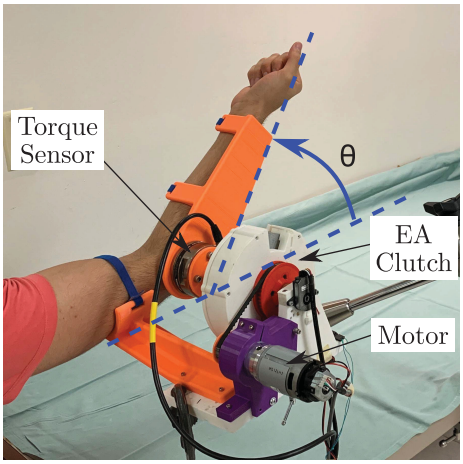

Fig. 14. Elbow rehabilitation exoskeleton validation setup.

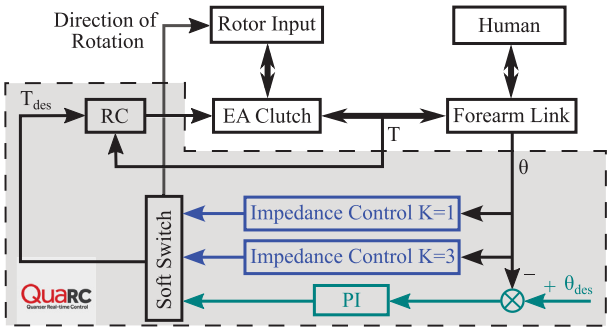

Fig. 15. Control system diagram. The blue path shows the impedance controller for active-resistive rehabilitation. The green path shows the PI controller of the coordination-assisted rehabilitation.

in open-loop and using the PI controller to compare with the RC. Fig. 13(a) shows the amplitude of the output torque in decibels. It can be seen that the implementation of the RC and PI controller improved the frequency response of the system. However, overshoots can be seen in the figure for frequencies close to 0.6 Hz for the PI controller. Negligible degradation in the amplitude was observed up to 1 Hz. This shows the potential of the EA clutch in HRI applications, which naturally have low bandwidth [40], [41]. Fig. 13(b) shows the absolute tracking error. As can be seen, the RC tracking error is much less than that of the PI controller.

Despite the mentioned benefits of the proposed system, there are some limitations which would motivate future research and development. The main limitations are as follows: (a) The acoustic noise of the system is rooted in the PWM drive. It is, therefore, necessary to investigate noise suppression/isolation methods in future research; (b) the optimization of the power consumption of the clutch was not investigated in this research; and (c) this study does not include the fatigue of such actuators and the changes in the dynamics over long-term use. Due to the physics of the system, it can be assumed that fatigue analysis would be an important line of future research.

VII. Rehabilitation Experiment and Discussion

In this section, the performance of the EA clutch for two different training modalities, i.e., active-resistive and coordination-assisted (trajectory guidance) rehabilitation [42], is validated.

A stationary elbow exoskeleton was made using the EA clutch, as shown in Fig. 14. The stator of the clutch was connected to the forearm link through an ATI gamma force/torque sensor. The arm and forearm of a healthy user were attached to the arm link and the forearm link, respectively, using Velcro straps. A DC motor was used to rotate the rotor of the clutch. Depending on the direction of the rotation of the rotor, the rehabilitation device can apply flexion and extension torques to the user's forearm. The rotation of the rotor in the direction of flexion of the forearm is assumed to be positive. An impedance controller and a PI controller were used in an outer loop control for resistive and coordination-assisted rehabilitation scenarios, respectively. A tangent hyperbolic function was used to switch between the control strategies without imposing high-frequency torques on the user's limb. Fig. 15 shows the diagram of the control system.

Authorized licensed use limited to: New York University. Downloaded on December 23,2022 at 06:14:04 UTC from IEEE Xplore. Restrictions apply.

Trajectory tracking error amplification is a paradigm of robotic rehabilitation for cases that can deliver muscle activity [34]. The user's neuro-musculoskeletal effort to minimize the trajectory tracking error reinforces the biceps and triceps muscles. In an active-resistive rehabilitation scenario, the robot applies a reactive torque field against the user's motion to increase the trajectory tracking error of the user [5], [43]. The user was asked to track a sinusoidal reference trajectory in this experiment while the robot actively applied a prescribed resistive virtual impedance. Soft (stiffness = 1 N.m/rad) and hard (stiffness = 3 N.m/rad) environments were implemented using the impedance control law given by

$$T_{des} = \begin{cases} -K(\theta - 10) & \theta \geq 10^\circ \quad (17a) \\ 0 & \theta < 10^\circ \quad (17b) \end{cases}$$

Although only a virtual spring was implemented in this experiment, damping and inertia can also be added to the control loop.

In a coordination-assisted rehabilitation scenario, the user's motion was assisted and coordinated with the robot to track a prescribed trajectory, and the user was asked to remain passive during the experiment. This type of exercise is designed for patients unable to activate their upper-arm muscles [35], [42], [43], [44]. The rotor of the clutch was rotated with positive constant velocity, and thus the robot applied a positive torque to move the user's forearm. A PI controller given by the equation below was used to coordinate the user's forearm on the prescribed trajectory (see Fig. 15)

$$T_{des} = \int K_I(\theta_{des} - \theta)dt + K_P(\theta_{des} - \theta) \quad (18)$$

where K_I and K_P were selected to be 10, and 3, respectively. Although impedance control and PI controllers both control positions in an outer loop and may be similar, these strategies differ fundamentally in two ways. First, the PI controller gets a desired trajectory to follow, but not the impedance controller. Second, the impedance controller can apply inertia (if we use all components of the virtual environment), which is not applicable using the PI (or a PID) controller. However, the integral term of the PI controller, which is necessary for a coordination-assisted scenario to compensate for gravity, does not have any meaning as "physical" impedance. Thus, the PI controller cannot represent impedance control.

Fig. 16 shows the results for the experiments. The area highlighted in blue shows the resistive rehabilitation with the soft environment. The region highlighted in red shows the resistive rehabilitation with the hard virtual environment, and the region highlighted in green shows the coordination-assisted rehabilitation. Fig. 16(a) shows the target trajectory and the measured forearm angle. Fig. 16(c) shows the desired torque, which is calculated by the outer loop controller (impedance controller in the active-resistive rehabilitation and the PI controller in the coordination-assisted rehabilitation scenario) and the rendered torque, which is controlled by the low-level RC. The negative torque refers to the effort of the robot in the extension of the forearm, and positive torque refers to the effort of the robot in the flexion of the forearm. As can be seen in the figure, the

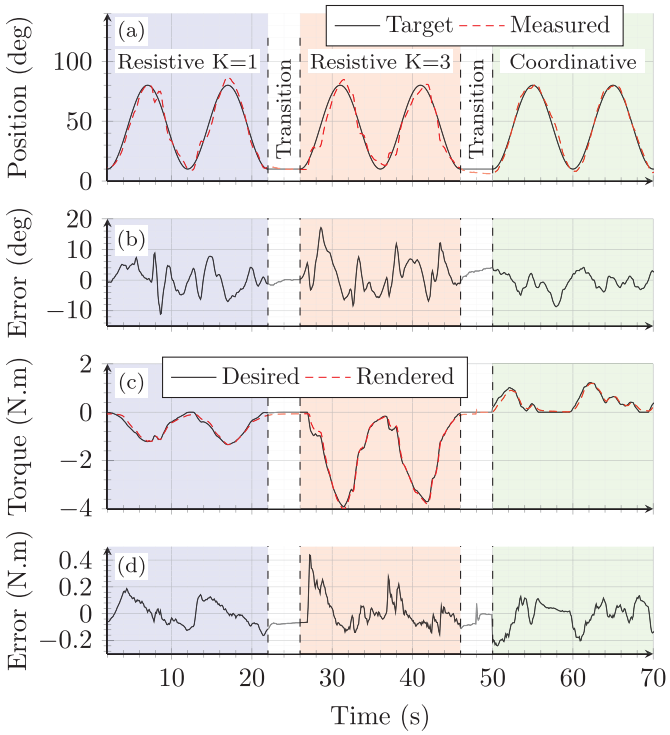

Fig. 16. Results of the rehabilitation training experiments. (a) Target and hand positions. (b) Position tracking error. (c) Desired and rendered interaction torque. (d) Torque tracking error.

rendered interaction torque perfectly follows the desired trajectory both in the active-resistive and coordination-assisted modalities.

Fig. 16(b) shows the position tracking error. As can be seen, the position tracking error increases with the increase of the environment stiffness in resistive rehabilitation. However, no remarkable difference can be seen in the torque tracking error between hard and soft environments, as shown in Fig. 16(d). This is the desired outcome, which is due to the high resistive force applied by the robot to the user's forearm. On the other hand, it can be seen that the position tracking error in coordination-assisted training is less than in resistive therapy since the robot assists in moving the user's forearm on the trajectory. These results can be seen more clearly in Fig. 17, which shows the box plot of the absolute position tracking error. The student's T-test was performed after the validation of the normality of the absolute tracking error of each experiment (p-value < 0.001 for all experiments). A significant absolute tracking error difference was observed between the results for experiments with different environment stiffness (p-value $= 0.001$) and between the results for resistive and coordination-assisted rehabilitation (p-value < 0.005 for both cases) experiments. These results demonstrate the desired performance of the proposed wearable rehabilitation device in increasing the position tracking error in target tracking resistive rehabilitation scenarios and manipulating the user's forearm in a coordination-assisted scenario.

The EA clutch has shown great potential for elbow assistive/resistive rehabilitation exoskeletons due to its inherent safety and ease of torque control. Due to the low power, high

Authorized licensed use limited to: New York University. Downloaded on December 23,2022 at 06:14:04 UTC from IEEE Xplore. Restrictions apply.

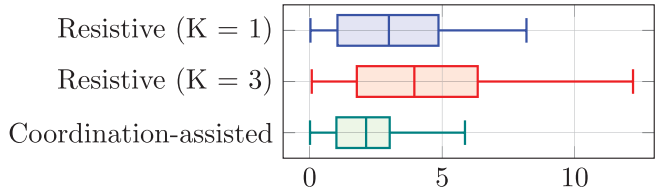

Fig. 17. Absolute position tracking error.

force density, and lightweight of the EA clutch, it is suitable for applications in wearable and mobile assistive devices such as exoskeletons and robotic walkers as an independent passive actuator [20] or along with a motor.

The weight of the test clutch used in this paper was around 450 g which includes a set of triple clutch discs that weighed around 30 g. This means, the torque capacity of the clutch can be easily increased by increasing the number of clutch discs without a substantial increase in the weight of the clutch, e.g., the torque can be increased to 20 N.m by adding 4 more sets of discs which would weigh around 120 g. Despite the low weight of the test clutch used due to the lightweight clutch discs, optimization of the weight of the clutch was not investigated and is a topic for future research.

VIII. Conclusion

An efficient high-fidelity robust control approach was presented to control an electroadhesive clutch. In the first step, the friction between the clutch plates was studied, and a nonlinear friction function was proposed to model the time-dependent behavior of friction. It was observed that the friction dynamics are nonlinearly dependent on the normal force. In order to control the clutch, a novel activation signal using a special bipolar PWM scheme was used to address the electroadhesion degradation issue, as well as to allow the duty cycle of the PWM signal to be adjusted to tune electroadhesion. Then, an accurate nonlinear model, and a simplified linear model were identified for estimating the torque from the control signal. A robust controller based on the simplified linear model was implemented, and the results were compared to a PI controller. The results showed that when using the robust control approach, the clutch follows a multi-sinusoidal trajectory more closely. The performance of the proposed control, along with an electroadhesive clutch as a semi-passive actuator, was experimentally validated in active-resistive and coordination-assisted rehabilitation scenarios. The results showed that this technology can be used in safe physical human-robot interaction systems, such as exoskeletons, rehabilitation, and assistive robots.

References

[1] A. Zacharaki, I. Kostavelis, A. Gasteratos, and I. Dokas, "Safety bounds in human robot interaction: A survey," *Safety Sci.*, vol. 127, Art. no. 104667, 2020.

[2] N. Feizi, M. Tavakoli, R. V. Patel, and S. F. Atashzar, "Robotics and AI for teleoperation, tele-assessment, and tele-training for surgery in the era of COVID-19: Existing challenges, and future vision," *Front. Robot. AI*, vol. 8, Apr. 2021, Art. no. 610677.

[3] C. Nicholson-Smith, V. Mehrabi, S. F. Atashzar, and R. V. Patel, "A multi-functional lower-and upper-limb stroke rehabilitation robot," *IEEE Trans. Med. Robot. Bionics*, vol. 2, no. 4, pp. 549–552, Nov. 2020.

[4] B. Noronha and D. Accoto, "Exoskeletal devices for hand assistance and rehabilitation: A comprehensive analysis of state-of-the-art technologies," *IEEE Trans. Med. Robot. Bionics*, vol. 3, no. 2, pp. 525–538, May 2021.

[5] C. Rossa, M. Najafi, M. Tavakoli, and K. Adams, "Robotic rehabilitation and assistance for individuals with movement disorders based on a kinematic model of the upper limb," *IEEE Trans. Med. Robot. Bionics*, vol. 3, no. 1, pp. 190–203, Feb. 2021.

[6] S. Mehrdad, F. Liu, M. T. Pham, A. Lelevé, and S. F. Atashzar, "Review of advanced medical telerobots," *Appl. Sci.*, vol. 11, no. 1, p. 209, 2020.

[7] S. F. Atashzar, M. Shahbazi, M. Tavakoli, and R. V. Patel, "A computational-model-based study of supervised haptics-enabled therapist-in-the-loop training for upper-limb poststroke robotic rehabilitation," *IEEE/ASME Trans. Mechatronics*, vol. 23, no. 2, pp. 563–574, Apr. 2018.

[8] T. B. Sheridan, "Human–robot interaction: Status and challenges," *Human Factors*, vol. 58, no. 4, pp. 525–532, 2016.

[9] T. Haidegger, "Autonomy for surgical robots: Concepts and paradigms," *IEEE Trans. Med. Robot. Bionics*, vol. 1, no. 2, pp. 65–76, May 2019.

[10] A. S. Shafer and M. R. Kermani, "On the feasibility and suitability of MR fluid clutches in human-friendly manipulators," *IEEE/ASME Trans. Mechatronics*, vol. 16, no. 6, pp. 1073–1082, Dec. 2011.

[11] S. V. Sarkisian, M. K. Ishmael, G. R. Hunt, and T. Lenzi, "Design, development, and validation of a self-aligning mechanism for high-torque powered knee exoskeletons," *IEEE Trans. Med. Robot. Bionics*, vol. 2, no. 2, pp. 248–259, May 2020.

[12] B. Vanderborght et al., "Variable impedance actuators: A review," *Robot. Auton. Syst.*, vol. 61, no. 12, pp. 1601–1614, 2013.

[13] N. Najmaei, A. Asadian, M. R. Kermani, and R. V. Patel, "Design and performance evaluation of a prototype MRF-based haptic interface for medical applications," *IEEE/ASME Trans. Mechatronics*, vol. 21, no. 1, pp. 110–121, Feb. 2016.

[14] S. Pisetskiy and M. Kermani, "High-performance magneto-rheological clutches for direct-drive actuation: Design and development," *J. Intell. Mater. Syst. Struct.*, vol. 32, no. 20, pp. 2582–2600, 2021.

[15] C. Khazoom, P. Caillouette, A. Girard, and J.-S. Plante, "A supernumerary robotic leg powered by magnetorheological actuators to assist human locomotion," *IEEE Robot. Autom. Lett.*, vol. 5, no. 4, pp. 5143–5150, Oct. 2020.

[16] J. Li, L. Zhao, and T. Li, "Robotic walker for slope mobility assistance with active-passive hybrid actuator," *Chin. J. Mech. Eng.*, vol. 34, no. 1, pp. 1–10, 2021.

[17] J. R. Davidson and H. I. Krebs, "An electrorheological fluid actuator for rehabilitation robotics," *IEEE/ASME Trans. Mechatronics*, vol. 23, no. 5, pp. 2156–2167, Oct. 2018.

[18] R. Chaichaowarat, S. Nishimura, and H. I. Krebs, "Macro-mini linear actuator using Electrorheological-fluid brake for impedance modulation in physical HumanRobot interaction," *IEEE Robot. Autom. Lett.*, vol. 7, no. 2, pp. 2945–2952, Apr. 2022.

[19] S. Pisetskiy and M. R. Kermani, "A concept of a miniaturized MR clutch utilizing MR fluid in squeeze mode," in *Proc. IEEE/RSJ Int. Conf. Intell. Robots Syst. (IROS)*, 2020, pp. 6347–6352.

[20] S. Diller, C. Majidi, and S. H. Collins, "A lightweight, low-power electroadhesive clutch and spring for exoskeleton actuation," in *Proc. IEEE Int. Conf. Robot. Autom. (ICRA)*, 2016, pp. 682–689.

[21] J. Guo, J. Leng, and J. Rossiter, "Electroadhesion technologies for robotics: A comprehensive review," *IEEE Trans. Robot.*, vol. 36, no. 2, pp. 313–327, Apr. 2020.

[22] D. M. Aukes et al., "Design and testing of a selectively compliant underactuated hand," *Int. J. Robot. Res.*, vol. 33, no. 5, pp. 721–735, 2014.

[23] S. B. Diller, S. H. Collins, and C. Majidi, "The effects of electroadhesive clutch design parameters on performance characteristics," *J. Intell. Mater. Syst. Struct.*, vol. 29, no. 19, pp. 3804–3828, 2018.

[24] K. Zhang, E. J. Gonzalez, J. Guo, and S. Follmer, "Design and analysis of high-resolution electrostatic adhesive brakes towards static refreshable 2.5D tactile shape display," *IEEE Trans. Haptics*, vol. 12, no. 4, pp. 470–482, Oct.–Dec. 2019.

[25] R. Hinchet and H. Shea, "High force density textile electrostatic clutch," *Adv. Mater. Technol.*, vol. 5, no. 4, 2020, Art. no. 1900895.

[26] V. Ramachandran, J. Shintake, and D. Floreano, "All-fabric wearable electroadhesive clutch," *Adv. Mater. Technol.*, vol. 4, no. 2, 2019, Art. no. 1800313.

Authorized licensed use limited to: New York University. Downloaded on December 23,2022 at 06:14:04 UTC from IEEE Xplore. Restrictions apply.

[27] V. Ramachandran, F. Schilling, A. R. Wu, and D. Floreano, "Smart textiles that teach: Fabric-based haptic device improves the rate of motor learning," *Adv. Intell. Syst.*, vol. 3, no. 11, 2021, Art. no. 2100043.
[28] A. Detailleur, S. Umans, H. Van Even, A. Pennycott, and H. Vallery, "Feasibility analysis of a self-reinforcing electroadhesive rotational clutch," in *Proc. IEEE/ASME Int. Conf. Adv. Intell. Mechatronics (AIM)*, 2021, pp. 478–483.
[29] O. Testoni, A. Bergamini, S. Bodkhe, and P. Ermanni, "A novel concept for adaptive friction damper based on electrostatic adhesion," *Smart Mater. Struct.*, vol. 29, no. 10, 2020, Art. no. 105032.
[30] T. Nakamura and A. Yamamoto, "Modeling and control of electroadhesion force in DC voltage," *Robomech J.*, vol. 4, no. 1, pp. 1–10, 2017.
[31] R. Chen et al., "Time-dependent electroadhesive force degradation," *Smart Mater. Struct.*, vol. 29, no. 5, 2020, Art. no. 55009.
[32] M. Graule et al., "Perching and takeoff of a robotic insect on overhangs using switchable electrostatic adhesion," *Science*, vol. 352, no. 6288, pp. 978–982, 2016.
[33] N. Feizi, S. F. Atashzar, M. R. Kermani, and R. V. Patel, "Design and modeling of a smart torque-adjustable rotary electroadhesive clutch for application in human-robot interaction," 2022, *arXiv:2210.08664*.
[34] L. Marchal-Crespo and D. J. Reinkensmeyer, "Review of control strategies for robotic movement training after neurologic injury," *J. Neuroeng. Rehabil.*, vol. 6, no. 1, pp. 1–15, 2009.
[35] C. Weiller et al., "Brain representation of active and passive movements," *Neuroimage*, vol. 4, no. 2, pp. 105–110, 1996.
[36] M. R. Kermani, R. V. Patel, and M. Moallem, "Friction identification and compensation in robotic manipulators," *IEEE Trans. Instrum. Meas.*, vol. 56, no. 6, pp. 2346–2353, Dec. 2007.
[37] M. W. Spong, S. Hutchinson, and M. Vidyasagar, "Multivariable control," in *Robot Modeling and Control*. Hoboken, NJ, USA: Wiley, 2006, pp. 263–279.
[38] B. Siciliano, L. Sciavicco, L. Villani, and G. Oriolo, *Robotics: Modelling, Planning and Control*. London, U.K.: Springer, 2009.
[39] M. A. Tavallaei, S. F. Atashzar, and M. Drangova, "Robust motion control of ultrasonic motors under temperature disturbance," *IEEE Trans. Ind. Electron.*, vol. 63, no. 4, pp. 2360–2368, Apr. 2016.
[40] N. Feizi, R. V. Patel, M. R. Kermani, and S. F. Atashzar, "Adaptive wave reconstruction through regulated-BMFLC for transparency-enhanced telerobotics over delayed networks," *IEEE Trans. Robot.*, vol. 38, no. 5, pp. 2928–2942, Oct. 2022.
[41] N. Hogan, "Controlling impedance at the man/machine interface," in *Proc. IEEE Int. Conf. Robot. Autom.*, 1989, pp. 1626–1627.
[42] S. F. Atashzar, M. Shahbazi, and R. V. Patel, "Haptics-enabled interactive neurorehabilitation mechatronics: Classification, functionality, challenges and ongoing research," *Mechatronics*, vol. 57, pp. 1–19, Feb. 2019.
[43] A. Basteris, S. M. Nijenhuis, A. H. Stienen, J. H. Buurke, G. B. Prange, and F. Amirabdollahian, "Training modalities in robot-mediated upper limb rehabilitation in stroke: A framework for classification based on a systematic review," *J. Neuroeng. Rehabil.*, vol. 11, no. 1, pp. 1–15, 2014.
[44] Z. Rajestari, N. Feizi, and S. Taghvaei, "Kinematic synthesis and optimization of continuous passive motion mechanisms for knee," in *Proc. 7th Int. Conf. Model., Simulat., Appl. Optim. (ICMSAO)*, 2017, pp. 1–6.

Navid Feizi (Graduate Student Member, IEEE) received the B.Sc. degree in mechanical engineering from Shiraz University, Shiraz, Iran, in 2016, and the M.Sc. degree in mechanical engineering from the Sharif University of Technology, Tehran, Iran, in 2019. He is currently pursuing the Ph.D. degree with the School of Biomedical Engineering (Mechatronics), Western University, London, ON, Canada.

He is currently a Research Assistant with Canadian Surgical Technologies and Advanced Robotics (CSTAR), London Health Sciences Centre, London, ON, Canada. He is also a Trainee in effective systems for procedure-specific healthcare simulation with CSTAR. His research interests include human–robot interactions, rehabilitation and surgical robotics, haptics, teleoperation, and smart actuators.

S. Farokh Atashzar (Senior Member, IEEE) received the Ph.D. degree in electrical and computer engineering from the University of Western Ontario, Canada, in 2017.

He is currently an Assistant Professor with New York University (NYU), New York, NY, USA, jointly appointed with the Department of Electrical and Computer Engineering and Mechanical and Aerospace Engineering. He is also affiliated with NYU WIRELESS, New York, and NYU Center for Urban Science and Progress, New York, and Leads Medical Robotics and Interactive Intelligent Technologies (MERIIT) Lab, NYU, and the activities of the Lab are funded by the U.S. National Science Foundation. Prior to joining NYU, he was a Postdoctoral Scientist with Imperial College London, U.K. His research interests include a human-machine interface, haptics, human-centered robotics, biosignal processing, deep learning, and nonlinear control. He was the recipient of several awards, including the 2021 Outstanding Associate Editor of IEEE ROBOTICS AND AUTOMATION LETTERS. He is an Associate Editor for IEEE TRANSACTIONS ON ROBOTICS and IEEE ROBOTICS AND AUTOMATION LETTERS.

Mehrdad R. Kermani (Member, IEEE) received the Ph.D. degree in electrical and computer engineering from the University of Western Ontario, London, ON, Canada, in 2005.

He is currently a Professor with the Department of Electrical and Computer Engineering and the Director of Advanced Robotics and Mechatronic Systems laboratory, Western University. His expertise and research interests include human–robot collaborations, robotic grasping, compliant actuations, agricultural robotics, and the use of smart materials for developing human-centric technologies in robotics. He has served as the Co-Chair of a number IEEE conferences, including ICRA and the selection panel of multiple funding agencies. He is currently an Associate Editor for the IEEE ROBOTIC AND AUTOMATION LETTERS.

Rajni V. Patel (Life Fellow, IEEE) received the Ph.D. degree in electrical engineering from the University of Cambridge, U.K., in 1973.

He is currently a Distinguished University Professor and a Tier-1 Canada Research Chair with the Department of Electrical and Computer Engineering, Western University, London, ON, Canada, with cross appointments in the Department of Surgery and the Department of Clinical Neurological Sciences, Western University. He is also the Director of Engineering with Canadian Surgical Technologies and Advanced Robotics, London Health Sciences Centre, London, ON, Canada.

Prof. Patel was on the editorial boards of the IEEE TRANSACTIONS ON ROBOTICS, the IEEE/ASME TRANSACTIONS ON MECHATRONICS, the IEEE TRANSACTIONS ON AUTOMATIC CONTROL, *Automatica*, and the *Journal of Medical Robotics Research* and is currently on the editorial board of the International *Journal of Medical Robotics and Computer Assisted Surgery*. He is a Fellow of the ASME, the Royal Society of Canada, and the Canadian Academy of Engineering.

Authorized licensed use limited to: New York University. Downloaded on December 23,2022 at 06:14:04 UTC from IEEE Xplore. Restrictions apply.